Biochemistry **2000,** *39,* 1499−1514

Structural Consequences of *b*- to *c*-type Heme Conversion in Oxidized *Escherichia coli* Cytochrome b_{562}[†,‡]

Fabio Arnesano, Lucia Banci, Ivano Bertini,* and Simone Ciofi-Baffoni

Magnetic Resonance Center CERM, University of Florence, Via Luigi Sacconi 6, 50019, Sesto Fiorentino, Florence, Italy

Thierry de Lumley Woodyear, Christopher M. Johnson, and Paul D. Barker*

Centre for Protein Engineering, MRC Centre, Hills Road, Cambridge CB2 2QH, United Kingdom

Received August 6, 1999; Revised Manuscript Received November 10, 1999

ABSTRACT: An NMR characterization of the 98Arg → Cys variant of iron (III)-containing cytochrome b_{562} from *Escherichia coli* has been performed and the solution structure obtained. This variant has a covalent bond between the heme and Cys 98, thus mimicking the heme binding in cytochrome *c*. The R98C cytochrome is shown to have a significantly increased stability, compared to that of wild type, toward thermal and chemical denaturation. In water at 20 °C it is 5.60 kJ mol^{-1} more stable than the WT protein, measured by equilibrium guanidine hydrochloride denaturation. The structure has been obtained through two-dimensional total correlation spectroscopy (TOCSY) and nuclear Overhauser effect spectroscopy (NOESY) experiments and through three-dimensional NOESY−^{15}N heteronuclear multiple quantum coherence (HMQC). By these methods, 85% of protons and 100% of backbone nitrogens were assigned. 2145 meaningful nuclear Overhauser effects (NOEs) (20 NOEs per residue), 45 backbone ^3J values, and 397 pseudocontact shifts were used to obtain a family of 35 members, which were then energy-minimized. The root-mean-square deviation (RMSD) with respect to the average structure is 0.50 ± 0.07 for the backbone and 1.01 ± 0.08 for the heavy atoms. The magnetic anisotropy resulting from analysis of the pseudocontact shifts indicates an anisotropy that is an intermediate between that of the wild-type, which is the smallest, and cytochrome *c*. The *g* values confirm a higher anisotropy of the variant with respect to the wild-type protein. The chirality of the heme 2α carbon is the same as that in all naturally occurring cytochromes *c*. The overall secondary structure and tertiary structure are very similar to the wild type. The removal of Arg 98 causes a change in the pH-dependent properties. The pK_a, proposed to be due to deprotonation of the coordinated histidine, is 1.5 units higher than in the wild type, consistent with the lack of the positive charge of Arg 98 close to the ionizable group. This is further support for the coordinated histidine being the titratable group with an alkaline pK_a in the wild-type protein. The pattern of the shifts of the heme methyl groups is different than in the wild-type protein, presumably due to alteration of the electronic structure by the presence of the covalent bond between the protein and the heme. The difference in stability between the variant and wild-type protein is discussed in terms of the structural information.

Heme is a cofactor found in virtually all organisms and is used for a variety of both electron transfer and catalytic processes. The protein structural and protein chemical factors that control the properties of the heme within proteins have been studied for many years (*1*, *2*). One type of protein−heme interaction that has received little attention is the covalent bond between the two, as found in cytochomes *c*. These proteins are characterized by the thioether linkages formed by the addition of cysteine thiol groups to the heme vinyl groups, in the sequence -CXXCH-. While the covalent attachment of the cofactor to the protein has the obvious consequence of determining essentially infinite affinity, neither the structural nor energetic response to this protein modification has been described for any heme binding system. The effect of the cofactor binding on stability and folding/unfolding properties has been the subject of recent work on a variety of heme proteins (*3*). In this context, the low-spin, six-coordinate electron-transfer proteins mitochondrial cytochrome *c* (*4*−*6*) and bacterial cytochrome b_{562} (*7*−*10*) have been extensively investigated. In the *b*-type cytochrome heme is noncovalently associated to the protein matrix. Two *b*-type cytochromes, b_5 and b_{562}, have been transformed into *c*-type cytochromes, through introduction of a single, *c*-type covalent linkage, and subsequently expressed in *Escherichia coli* (*11*, *12*). We can therefore compare the properties of proteins that differ only in the attachment of heme to protein. In the context of cytochrome

---

[†] This work was supported by the European Community (TMR-LSF Contract ERBFMGECT950033 and TMR Contract FMRX-CT98-0230), by Italian CNR (Progetto Finalizzato Biotecnologie 99.00509.PF49), and by MURST ex 40%. P.D.B. thanks the BBSRC for an Advanced Fellowship.

[‡] The average minimized structure is available at the Protein Data Bank: PDB entry 1QQ3 and RCSB entry RCSB009166.

* Corresponding authors. I.B.: Fax +39 055 4209271; Tel +39 055 4209272; E-mail bertini@CERM.UNIFI.IT. P.D.B.: Fax 01223 402140; Tel 01223 402130; E-mail pxb@mrc-lmb.cam.ac.uk.

10.1021/bi991831o CCC: $19.00

b_{562}, this aspect is particularly interesting because it is the only member of a family of four-helix bundle cytochromes not to have a covalently linked heme. The other members of the structurally homologous family, cytochromes c' and c_{556} from photosynthetic bacteria, all have heme attached to the CXXCH motif in the C-terminal helix (*13*).

To build up a detailed understanding of the energetics of the interactions between protein and metal cofactors, structural information is an essential starting point. The solution structure of metalloproteins determined by NMR is most useful for these studies. Structures of the oxidized low-spin heme proteins mitochondrial cytochrome *c*, microsomal cytochrome b_5 (*14* and references therein), and bacterial cytochrome b_{562} (*15*) have been determined. The studies on the *b*-type cytochromes highlight the power of NMR methods for examining the structure of various components in a mixture of species differing in some conformational properties (*16*−*18*). In particular, the two *b*-type cytochromes in question exist in two forms that differ in the orientation of the heme, which is rotated by 180° about the $\alpha-\gamma$ *meso* axis (*19*, *20*).

In the case of cytochrome $b_{562,}$ the variant Arg98Cys can be expressed and the heme attached to the cysteine thiol through the 2-vinyl group with the heme in the A orientation (*11*). This artificial, hybrid cytochrome is now being investigated with the aim of obtaining information on the role of the covalent bond on the heme properties and the protein stability. We have established methods for performing the heme attachment in vitro (*21*) and can therefore prepare significant quantities of this protein, isotopically labeled as required, for structure elucidation. While this protein does not exhibit the heme orientational disorder observed in the WT protein, all preparations we have made to date contain various amounts, minor in concentration, of a closely related species that differs in mass by +32 Da (*11*), the origin of which is still currently unknown. The high-resolution structure of the lower mass species with a normal *c*-type covalent linkage has been obtained from ^{15}N labeled samples containing both species. We report here the solution structure of the oxidized Arg98Cys cytochrome b_{562} (R98C cyt b_{562} hereafter)[1] and compare it with that of the wild-type protein as well as those that have been obtained from cytochromes *c* and c'.

MATERIALS AND METHODS

Sample Isolation and Preparation. Expression and purification of the Arg98Cys variant of cytochrome b_{562} was performed as described (*11*) with the following modifications. Expression from the plasmid pCEb562 was achieved in the *E. coli* strains TG2 or BL21(DE3)C41 (*22*) in 660 mL of 2× YT medium in a 2 L flask shaken at 250 rpm at 37 °C. For uniform isotopic labeling with ^{15}N, growth was in M9 minimal medium containing $^{15}NH_4Cl$ as the sole nitrogen source. To increase the yield of the covalently bound species, we have found conditions that result in the correct covalent bond being formed *in vitro*. These are described elsewhere for a double variant R98C/H102M cytochrome b_{562} (*21*) but require saturation of the apoprotein in the periplasm extract with exogenous (unlabeled) hemin. Unlike that protein, however, the same conditions result in only ~50% yield of covalently attached R98C variant. The separation of the protein with covalently attached heme from protein containing noncovalently attached heme was achieved by extraction of noncovalently bound heme by the acidic butan-2-one method (*23*) before final purification on Mono-Q anion-exchange columns. On a 10−100 mg scale this procedure was more efficient than the chemical modification method described previously (*11*).

For EPR and NMR samples were dissolved in phosphate buffer 0.5 M, pH 4.8, in D_2O or in 90% H_2O/D_2O.

Chemical Denaturation. Equilibrium denaturant unfolding studies of the WT and R98C ferricytochromes b_{562} were carried out with guanidine hydrochloride (GdnHCl, ICN Biomedicals, Inc.) as the denaturant. The optical spectra were followed as a function of denaturant concentration at 20 °C and pH 5. The protein concentration was around 5 μM. Spectra were obtained between 200 and 1100 nm with a Hewlett-Packard 8453 spectrophotometer. Denaturation curves were generated from the absorbance at single wavelengths. These curves were fitted to a two-state transition model (eq 1), with first-order baseline corrections where appropriate, using a nonlinear least-squares fitting routine to solve for *m* and $[\mathrm{GdnHCl}]_{1/2}$:

$$\Delta G_{\mathrm{D-N}} = -\mathrm{RT} \ln K = -RT \ln [(A_{\mathrm{N}} - A)/(A - A_{\mathrm{D}})]$$

where $\Delta G_{\mathrm{D-N}}$ is the free energy of unfolding, K is the

$$= \Delta G^{\circ}_{\mathrm{D-N}} - m[\mathrm{GdnHCl}]_{1/2} \qquad (1)$$

equilibrium constant, A is the observed absorbance, and A_{N} and A_{D} are the absorbance of the native and denatured states, respectively. $[\mathrm{GdnHCl}]_{1/2}$ represents the concentration of guanidine hydrochloride at which equal concentrations of native and denaturated forms are present. m is the slope for the dependence of $\Delta G_{\mathrm{D-N}}$ with [GdnHCl].

Calorimetry. Differential scanning calorimetry (DSC) was carried out on a Microcal VP-DSC instrument in 20 mM acetate or phosphate buffers at either pH 5 or 7 adjusted to an ionic strength of 0.1 M with KCl. Freshly oxidized samples (30−100 μM) of either WT or R98C cytochrome b_{562} were exchanged into the calorimetry buffer by gel filtration. Samples were degassed by stirring under vacuum and then placed in the calorimeter. Scans were performed between 20 and 130 °C at 60 °C/h. Reference scans of buffer alone were subtracted from the scans of protein samples.

NMR Spectroscopy. The NMR spectra were acquired on Avance 800 and 600 and DRX 500 Bruker spectrometers operating at a nominal frequencies of 800.13, 600.13, and 500.13 MHz, respectively. A QXI probe was used on the Avance 800 spectrometer, and a triple-resonance 5-mm probe was used on both 600 and 500 MHz spectrometers.

A TOCSY (*24*, *25*) spectrum was recorded on the 600 MHz spectrometer with a spin-lock time of 60 ms, a recycle time of 1.5 s, and a spectral window of 12 ppm.

---

[1] Abbreviations: cyt b_{562}, cytochrome b_{562}; R98C cyt b_{562}, Arg98Cys variant of cytochrome b_{562}; RMSD, root-mean-square deviation; EPR, electron paramagnetic resonance; TOCSY, total correlation spectroscopy; NOE, nuclear Overhauser effect; NOESY, nuclear Overhauser effect spectroscopy; HMQC, heteronuclear multiple quantum coherence; INEPT, insensitive nuclei enhanced by polarization transfer; WATERGATE, water suppression by gradient-tailored excitation; TPPI, time-proportional phase incrementation; WEFT, water eliminated Fourier transform.

A three-dimensional (3D) NOESY−^{15}N HMQC (*26*) experiment was recorded in H_2O solution with 256(^{1}H) × 128(^{15}N) × 2048(^{1}H) data points on the 600 MHz spectrometer. In this experiment the INEPT delay was set to 5.4 ms, the mixing time was 100 ms, and the carrier frequency was set in the center of the amide proton region, at 7.35 ppm. Spectral windows for the direct ^{1}H dimension and the indirect ^{1}H and ^{15}N dimensions were 21.0, 21.0, and 29.0 ppm, respectively.

Two-dimensional (2D) NOESY maps (*27*, *28*) (obtained on the H_2O and the D_2O samples) were acquired on the 800 MHz spectrometer with a mixing time of 100 ms, a recycle time of 500 ms, and a spectral window of 14 ppm. In addition, to detect connectivities between hyperfine-shifted signals, a 2D NOESY experiment (*27*, *28*) with a spectral width of 50 ppm in both frequency dimensions, with 30 ms of mixing time, and with a recycle time of 200 ms was acquired on the 500 MHz spectrometer. Connectivities involving the hyperfine-shifted broad signals of the iron axial ligands were detected through one-dimensional (1D) NOEs, recorded on the H_2O and the D_2O samples, using the reported methodology (*29*), by irradiating the signals at −5.9, −15.2, and −22.3 ppm. Detection of broad signals was enhanced by acquiring spectra with the SuperWEFT pulse sequence (*30*, *31*), using very short recycle times (<100 ms).

The HNHA experiment (*32*) was performed at 800 MHz to determine $^3J_{HNH\alpha}$ coupling constants. These were used to obtain constraints for ϕ torsion angles. The spectrum was recorded as a 128(^{1}H) × 80(^{15}N) × 2048(^{1}H) data set with pulsed field gradients (PFG) along the z axis. The mixing time was 100 ms. Spectral windows for the direct ^{1}H dimension and the indirect ^{1}H and ^{15}N dimensions were 12.0, 12.0, and 45.0 ppm, respectively.

For all the experiments, quadrature detection in the indirect dimensions was performed in the TPPI mode (*28*), and water suppression was achieved through the WATERGATE sequence (*33*), except in the NOESY experiments performed to detect connectivities between paramagnetically shifted resonances, where presaturation was used. All 2D data consisted of 4K data points in the acquisition dimension and of 1K experiments in the indirect dimension.

A series of 1D ^{1}H NMR spectra at 13 different temperatures was recorded on the Avance 800 NMR spectrometer, increasing the temperature by 5 degrees each step, from 273 to 333 K, to characterize the temperature dependence of the resonances of the paramagnetically shifted signals. As well, a series of 1D ^{1}H NMR spectra was collected at 600 MHz by varying the pH values from 3 to 10, to characterize the pH-dependent behavior. The shifts of two methyl groups have been simultaneously fitted to an equation with two pK_a values.

All 3D and 2D spectra were collected at 298 K, processed using the standard Bruker software (XWINNMR), and analyzed on IBM RISC 6000 computers using the XEASY program (*34*).

EPR Spectroscopy. EPR measurements were made with Bruker ER-200D spectrometer fitted with an in-house-designed He flow system (*35*) operating at a microwave frequency of 9411 MHz. In the EPR measurements the microwave power was 0.8 mW, the modulation frequency and amplitude were 100 kHz and 0.63 mT, respectively, and the temperature was 15.5 K. The EPR spectra simulations were based on a g-strain-broadened $S = {}^1/_2$ system (*36*).

Constraints Used in Structure Calculations. The majority of the peaks used for the structure calculations (≈90%, see later) were integrated in the NOESY map acquired over the diamagnetic window at 298 K in H_2O. Dipolar connectivities involving hyperfine-shifted protons were integrated in the 2D NOESY spectrum acquired over the 50 ppm spectral window. Intensities of dipolar connectivities were converted into upper distance limits, to be used as input values for structure calculations, using the program CALIBA (*37*). Connectivities measured in NOESY maps acquired with different mixing times were calibrated simultaneously using a scaling factor for the intensities of well-defined and isolated peaks in one spectrum with respect to the other. The calibration curves were adjusted iteratively as the structure calculations proceeded. The proton−proton distance constraints derived from 1D NOEs were introduced as upper distance limits of 5.0 Å. Stereospecific assignments of diastereotopic protons were obtained with the program GLOMSA (*37*).

$^3J_{HNH\alpha}$ coupling constants were used as constraints in the PSEUDYANA calculations. These coupling constants were correlated to the backbone torsion angle ϕ by means of the appropriate Karplus curve (*32*), given a ±2 Hz uncertainty in their values.

Hydrogen-bond constraints were introduced for backbone amide protons that were observed to be nonexchanging in D_2O solution after 3 days, and were found to be within hydrogen-bond distance and to have the correct orientation with respect to hydrogen-bond acceptors in structural models obtained without inclusion of these constraints. The distance between the NH proton and the hydrogen-bond acceptor was constrained to be in the 1.8−2.4 Å interval by inclusion of the corresponding upper and lower distance limits in structure calculations. In addition, upper and lower distance limits of 3.0 and 2.7 Å between the N and the acceptor atoms were also included. No H-bond constraints were introduced for nonexchanging NH protons for which it was not possible to unambiguously identify the corresponding acceptor.

Pseudocontact shifts (pcs hereafter) were used as additional constraints in structure calculations (*38*−*40*). The pcs were obtained by subtracting from the observed chemical shifts of the oxidized form of the variant R98C cyt b_{562} the shifts of the reduced form, estimated for the WT protein (*15*). A tolerance of 10% for the pcs constraints was used in the PSEUDYANA calculations (*41*) (see later) with a minimum value of 0.5 ppm for all protons. The hyperfine shifts of the heme, of the axial heme ligands (Met 7 and His 102) and of the mutated residue Cys 98 were not included in the calculations since they can experience a nonnegligible contact shift.

Structure Calculations. The structure calculations were performed with PSEUDYANA (*41*), which is a modified version of the program DYANA (*42*) adapted to include pcs as additional restraints. A preliminary family of 20 conformers obtained from only the NOE constraints was used as an input model for the program FANTASIAN (*43*, *44*) to estimate the initial values of $\Delta\chi_{ax}$ and $\Delta\chi_{rh}$, taken as starting values in the PSEUDYANA structure calculations. No assumption was made on the location of the heme group and the iron(III) ion. These were determined only by the

NOEs and the pcs, respectively. An upper distance limit of 0.2 Å was set between the pseudoatom defining the origin of the magnetic anisotropy tensor and the iron atom of the heme residue. The location of this residue and the tensor orientation were optimized during the structure calculations. Three cycles were needed to reach convergence, until the final values of $\Delta\chi_{ax}$ and $\Delta\chi_{rh}$ did not deviate more than 5% from the initial ones.

The modified heme group was included in the calculations by defining a new residue in the amino acid library built like a hybrid between *c*- and *b*-type hemes with an ethyl group at position 2 and a vinyl group at position 4. The two axial ligands (Met 7 and His 102) were linked to the iron atom through the sulfur atom of Met 7 and with the Nϵ2 of His 102 with upper distance limits of 2.34 and 2.10 Å, respectively. The sulfur atom of Cys 98 was linked to the 2-Cα of the heme through an upper distance limit of 2.1 Å. This approach does not impose any fixed orientation of the axial ligands with respect to the heme.

In all structure calculations, the relative weight of all classes of constraints (NOE, pcs, and *J* couplings) was fixed to the default PSEUDYANA value. Two hundred random conformers were annealed in 10 000 steps with the above constraints. The 35 conformers with the lowest target function constitute the final family.

Restrained energy minimization (REM) was then applied to each member of the family by use of the AMBER 5.0 package (*45*). The distance constraints were applied within the molecular mechanics and dynamics module of SANDER, and the pseudocontact shifts were included as constraints by means of the module PCSHIFTS (*44*). The force-field parameters for the heme and its ligands, as well as the overall calculation procedure, were set up following a procedure similar to that previously reported for heme proteins (*16*, *46*). The initial values of the magnetic susceptibility anisotropy used as input in these calculations were the values obtained for the final PSEUDYANA family. On this final PSEUDOREM family the magnetic susceptibility anisotropy parameters deviate less than 5% from their initial values (i.e., before energy minimization).

The program CORMA (*47*), which is based on relaxation matrix calculations, was used to back-calculate the NOESY cross-peaks and to check the validity of the structure. It has been also used to assign a few more cross-peaks between already assigned resonances.

The quality of the structure was evaluated in terms of deviations from ideal bond lengths and bond angles and through Ramachandran plots obtained by use of the programs PROCHECK (*48*) and PROCHECK-NMR (*49*).

Structure calculations and analyses were performed on IBM RISC 6000 computers.

RESULTS

Stability of R98C Ferricytochrome b_{562}. Optical spectra of R98C ferricytochrome b_{562} in the native and denatured state, obtained by addition of GdnHCl up to a concentration of 7.2 M, are shown in Figure 1A. Representative equilibrium denaturation curves for oxidized R98C and WT cyt b_{562} are shown in Figure 1B. The normalized absorbance at the wavelength maximum of the Soret band for each protein in its native state is plotted as a function of the concentration of GdnHCl. These data were fitted to eq 1, which describes a simple two-state transition process. The parameters for the least-squares fit to these data are given in Table 1. Also reported are the ΔG_{D-N} values extrapolated in the absence of denaturant (i.e., ΔG°_{D-N}) and at 3 M denaturant, assuming a two-state transition and that the *m*-value is constant with [GdnHCl]. At 20 °C in pH 5 buffer, the variant is therefore 5.6 kJ mol^{-1} more stable than the WT protein. In 3 M GdnHCl, $\Delta\Delta G_{D-N}$ is 22.6 kJ mol^{-1}. The T_m values measured by DSC for the thermal unfolding of the two proteins at pH 5 and 7 are also given in Table 1.

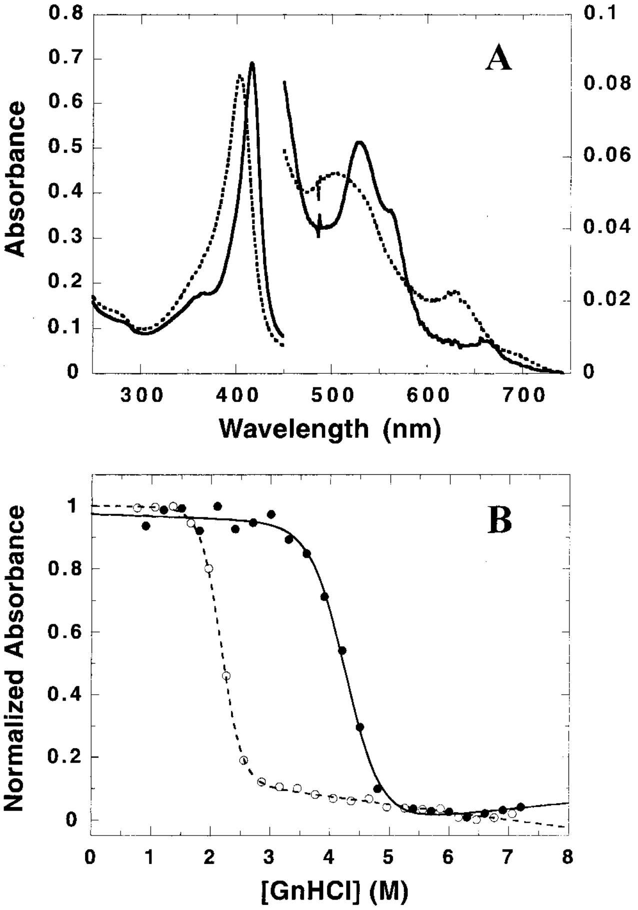

FIGURE 1: (A) Optical spectra of 4.8 μM R98C ferricytochrome b_{562} in 20 mM acetate, pH 5.0, containing of 0 (solid line) and 7.15 M (dotted line) guanidine hydrochloride (GdnHCl). The left-hand *y*-axis scale applies to wavelengths 250−450 nm. The right-hand axis applies to wavelengths 450−750 nm. (B) Denaturation curves for oxidized WT (○) and R98C (●) cyt b_{562} in GdnHCl. The absorbance values at the wavelength maximum of the Soret band in each of the native states (i.e., 418 nm for WT, 416 nm for R98C) were normalized and plotted against [GdnHCl]. The lines describe the least-squares fit to a function describing the equilibrium between two states with linear dependence upon [GdnHCl].

The spectrum of the R98C variant in 7.2 M GdnHCl (Figure 1A) is significantly different than that of the WT protein under the same conditions (not shown) (*3*), the latter being qualitatively similar to the spectrum of the free heme with a broad Soret band maximum and an extinction coefficient of ∼40 000 M^{-1} cm^{-1} at 380 nm. The Soret band of the denatured R98C variant (Figure 1A) has a maximum at 404 nm and an extinction coefficient of 140 000 M^{-1} cm^{-1}. In the visible region, maxima are observed at 507 and 630 nm.

Table 1: Parameters Characterizing the Unfolding of Oxidized Cyt b_{562} Proteins, by Guanidine Hydrochloride Denaturation Followed by Absorbance Spectroscopy, and the Thermal Denaturation Measured by Differential Scanning Calorimetry

protein	$[\text{GdnHCl}]_{1/2}{}^{a}$ (M)	m^{a} (kJ mol^{-1} M^{-1})	$\Delta G°_{\text{D-N}}{}^{b}$ (kJ mol^{-1}) at 0 M GdnHCl	$\Delta G_{\text{D-N}}{}^{b}$ (kJ mol^{-1}) at 3 M GdnHCl	T_m (°C) at pH 5	T_m (°C) at pH 7
WT	2.15 (2)	14.2 (2)	30.0 (4)	−12.1 (4)	73	67
R98C	4.27 (4)	8.4 (2)	35.6 (8)	10.5 (8)	97	87

[a] Parameters were obtained from the fitting of data collected at pH 5 to eq 1. The numbers in parentheses in the table are the errors in the last significant figure of the preceding numbers. [b] $\Delta G_{\text{D-N}}$ is the free energy for the denatured (D)−native (N) transition process, estimated at pH 5.

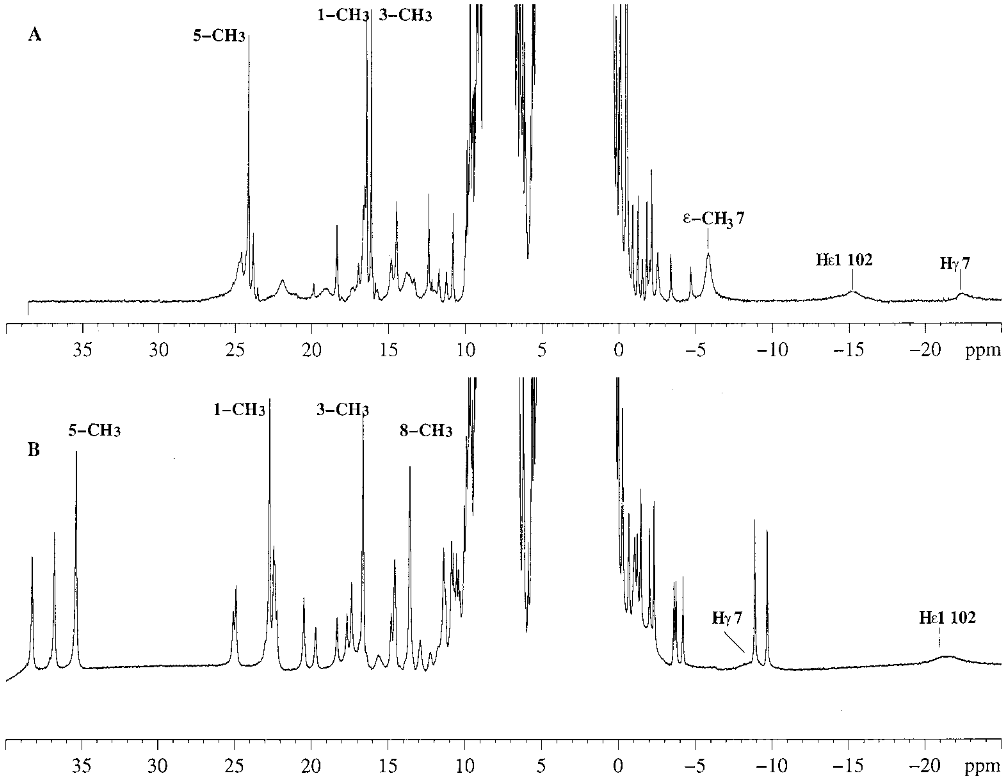

FIGURE 2: ^{1}H NMR spectra (800 MHz) of oxidized R98C cyt b_{562} (A) and WT cyt b_{562} (B) proteins at 298 K and pH = 4.8 in 500 mM phosphate buffer. The protein concentrations were 3 mM.

Paramagnetically Shifted Signals. The ^{1}H NMR spectrum of the oxidized form of R98C cyt b_{562} in 500 mM phosphate buffer at pH = 4.8 is shown in Figure 2A. The present oxidized form contains a low-spin iron(III) species, which is paramagnetic and therefore affects the NMR resonances (*50, 51*). The spectrum exhibits several upfield- and downfield-shifted signals with different intensity ratios. The spectrum is significantly different from that of the wild-type protein (Figure 2B), as far as the paramagnetically shifted signals are concerned (*11, 15, 51*).

In the WT protein two species, in which the orientation of the heme group differs by a 180° rotation around the α−γ axis, are present in the ratio of 2:1 and are referred to as forms A and B, respectively (*51*). In this variant, the heme is covalently attached to the protein frame through a thioether linkage between the sulfur atom of Cys 98 and the position 2 on the heme ring. Nevertheless, the NMR spectra of the variant provide evidence of the presence of a further minor form with an intensity ratio of 1:10 to the major form. Mass spectrometry has shown that R98C cyt b_{562} contains two forms characterized by a difference in mass of 32 Da (*11*). In any case, the presence of a minor form (cyt b_{562} + 32 Da) did not prevent assignment of the major form, which is the species studied in the present paper.

Suitable experiments were performed for the assignment of all the signals affected by the paramagnetic center, including those falling in the diamagnetic region. A 2D NOESY experiment was recorded with a short mixing time on a large spectral window, optimized for the detection of connectivities among fast-relaxing signals. This spectrum has been used to assign the heme resonances and some other paramagnetically shifted signals from protons of residues in the proximity of the heme. The assignment of the broad hyperfine-shifted signals of the axial iron ligands was achieved by 1D NOEs experiments. One Hγ proton of the axial Met was assigned to the signal at −22.3 ppm, the ϵ-CH$_3$ was assigned to the signal at −5.9 ppm, and the Hϵ1 proton of the axial His was assigned to the signal at −15.2 ppm, on the basis of their NOE connectivities. When this last signal is saturated in the H$_2$O sample, NOE connectivities have been observed with the resonances of the His102 β-protons and with a broad signal at 7.5 ppm. Performing the same experiment on the D$_2$O sample, the above-mentioned connectivities were no longer observed, while NOEs connectivities with the 1- and 8-methyl resonances appeared. This behavior can be interpreted as an effect of second-order NOE magnetization transfer from the Hϵ1 proton of His102 to its β protons, through Hδ1 imidazole proton of the His 102,

Table 2: Separation of Contact and Pseudocontact Contributions to the Hyperfine Shift in Oxidized *E. coli* R98C Cyt b_{562} at 298 K[a]

atom name	residue name	chemical shift ox R98C cyt b_{562} (ppm)	chemical shift red R98C cyt b_{562} (ppm)[b]	hyperfine shift R98C cyt b_{562} (ppm)	calculated pseudocontact shift R98C cyt b_{562} (ppm)	contact shift R98C cyt b_{562} (ppm)	calculated pseudocontact shift WT cyt b_{562} (ppm)	contact shift WT cyt b_{562} (ppm)	contact shift ox hh cyt c[c] (ppm)
HN	Met 7	12.32	na[d]		3.8 ± 0.8		1.3 ± 0.3	2.6	
Hα	Met 7	14.72	1.63	13.09	10.9 ± 1.3	2.2	5.7 ± 1.2	−2.8	−0.3
Hβ2/Hβ3	Met 7	16.56	0.22/−2.52	16.34/19.08	2.1 ± 1.2	14.2/17.0	−0.5 ± 2.0	14.0	
Hγ2/Hγ3	Met 7	−22.3	−1.40/−3.18	−20.9/−19.12	6.7 ± 1.3	−27.6/−25.8	3 ± 3	−9.0	
ϵ-CH$_3$	Met 7	−5.9	−2.90	−3.0	6.2 ± 2.8	−9.2	6.5 ± 4.5	−9.8	−25.8
HN	Cys 98	7.21	na		−0.29 ± 0.2				
Hα	Cys 98	3.49	na		−1.3 ± 0.8				
Hβ2/Hβ3	Cys 98	3.10/2.78	na		−0.51 ± 0.5				
HN	His 102	10.74	na		2.9 ± 0.6		0.8 ± 0.2	3.7	
Hα	His 102	8.74	na		4.7 ± 1.0		2.1 ± 0.4		1.0
Hβ2/Hβ3	His 102	23.73/18.28	na		4.4 ± 0.2		2.9 ± 0.2		2.1/7.5
Hδ1	His 102	7.5	na		5.8 ± 1.0		6.0 ± 0.5	1.9	−6.0
Hδ2	His 102	na	na		19.2 ± 3.9		2.8 ± 1.6		−1.2
Hϵ1	His 102	−15.2	na		3.5 ± 3.1		13 ± 5	−32.5	−39.0
8-CH$_3$	heme	8.26	3.67	4.59	−1.8 ± 0.3	6.4	−2.4 ± 0.7	12.4	35.4
meso-δH	heme	8.31	9.83	−1.52	−3.7 ± 0.5	2.2	−2.5 ± 0.7	4.6	2.1
1-CH$_3$	heme	16.4	3.41	12.99	−1.4 ± 0.1	14.4	−0.3 ± 0.3	19.6	7.7
2-Hα	heme	0.50	5.97	−5.47	−3.1 ± 0.9	−2.4	−0.8 ± 0.2	15.0	−1.8
2-βCH$_3$	heme	−0.92	2.28	−3.2	−1.9 ± 0.7	−1.3			−1.0
meso-αH	heme	−2.52	9.14	−11.66	−7.8 ± 0.9	−3.9	−4.4 ± 0.25	−1.3	−1.6
3-CH$_3$	heme	16.10	2.50	13.6	−2.7 ± 0.2	16.3	−2.7 ± 0.1	15.6	30.1
4-Hα	heme	6.87	8.30	−1.43	−1.4 ± 0.5	−0.03	−1.7 ± 0.2	2.0	−1.5
4-Hβ (*trans*)	heme	−0.58	4.48	−5.06	−1.0 ± 0.1	−4.1	−1.5 ± 0.2	−6.5	
4-Hβ (*cis*)	heme	−1.85	5.68	−7.53	−1.8 ± 0.2	−5.7	−0.96 ± 0.07	−5.0	
meso-βH	heme	7.17	9.93	−2.76	−3.9 ± 0.4	1.1	−3.2 ± 0.5	−4.8	0.13
5-CH$_3$	heme	24.12	3.81	20.31	−1.5 ± 0.1	21.8	−0.5 ± 0.4	32.5	11.0
meso-γH	heme	0.48	9.74	−9.26	−7.5 ± 0.2	−1.8			4.1

[a] For comparison, data for WT cyt b_{562} and horse heart (hh) cyt *c* are also reported. [b] Taken from ref *11*. [c] Taken from ref *46*. [d] Not assigned.

which provides the resonance at 7.5 ppm. As this latter HN proton is exchanging in the D_2O sample, the second-order NOEs connectivities are not detected, while the actual connectivities of Hϵ1 proton can be detected due to the improved signal-to-noise ratio in D_2O solutions. The complete assignment of the paramagnetically shifted signals is reported in the first three columns of Table 2. Comparison between the shifts of the heme resonances of the variant and of the native protein reveals that the heme resonances of the variant experience, on average, smaller shifts than the native protein, indicating some changes in the electronic structure of the paramagnetic center.

The temperature dependence of the paramagnetically shifted signals in R98C cyt b_{562} is essentially similar to that already reported for the native protein (*51*). As shown in Figure 3, most of the signals show a curvature in their temperature dependence, in some cases very steep. Some of them, like the heme methyl groups and the propionates Hα, follow anti-Curie behavior, while signals such as the Hβ protons of His 102 and the amide protons of Met 7 and His 102 exhibit Curie-like behavior. The ϵ-CH$_3$, Hγ, and Hβ protons of Met 7 follow a Curie behavior at low temperature, while at higher temperatures a gradual increase of the hyperfine shift was observed, indicating "hyper-Curie" behavior. This behavior was interpreted, in the case of the WT protein, as being due to the occurrence of spin equilibrium between $S = {}^{1}/_{2}$ and $S > {}^{1}/_{2}$ states (*51*, *52*). At variance with NMR, EPR spectra at 15 K detect only a single species (see later). By looking in detail at the temperature-dependence plots of heme methyl resonances and of some hyperfine-shifted signals belonging to the axial ligands, for both the WT protein and the variant, it is possible to make a comparison. The 1-, 5-, and 8-CH$_3$ resonances show the same curvature in both cases but the shifts are higher in WT cyt b_{562}. The 3-CH$_3$ in WT cyt b_{562} displays a higher curvature and a larger shift variation with respect to R98C cyt b_{562}. For the β protons of His102, the behavior is very similar in the two cases, while the Hϵ1 is shifted further upfield in the WT protein and experiences a larger shift variation in comparison to the variant. The β protons of Met 7 in the variant have the same curvature and larger downfield shifts. The ϵ-CH$_3$ and the Hγ protons of Met 7 in the WT protein are less shifted upfield than in the variant and their variation with temperature is more evident.

The shifts of paramagnetic signals of the present variant R98C cyt b_{562} have been monitored by pH titration, and two pK_a constants have been found by fitting the shift variations for 3-CH$_3$ and 5-CH$_3$ signals simultaneously (Figure 4A). The pK_a values are 5.7 and 9.6. For the WT protein the fitting analysis gives pK_a values of 5.8 and 8.1 (Figure 4B).

Sequence-Specific Assignment. Assignments of the signals falling in the diamagnetic region were performed by 3D NOESY−^{15}N HMQC and 2D NOESY and TOCSY. The 3D map was used to assign ^{15}N and proton resonances for all residues. The first assigned residues were glycines, due to their specific ^{15}N chemical shifts, and threonines, alanines, and valines, as they have easily recognizable spin patterns. These residues were connected to other spin patterns by sequential characteristic NOESY peaks. At this stage, the assignment work was aided by using preliminary structure calculations and the paramagnetic NOESY spectrum in which proton resonances of residues close to the metal center were identified. All the 106 residues have been assigned. About 85% of the proton resonances could be located in the maps,

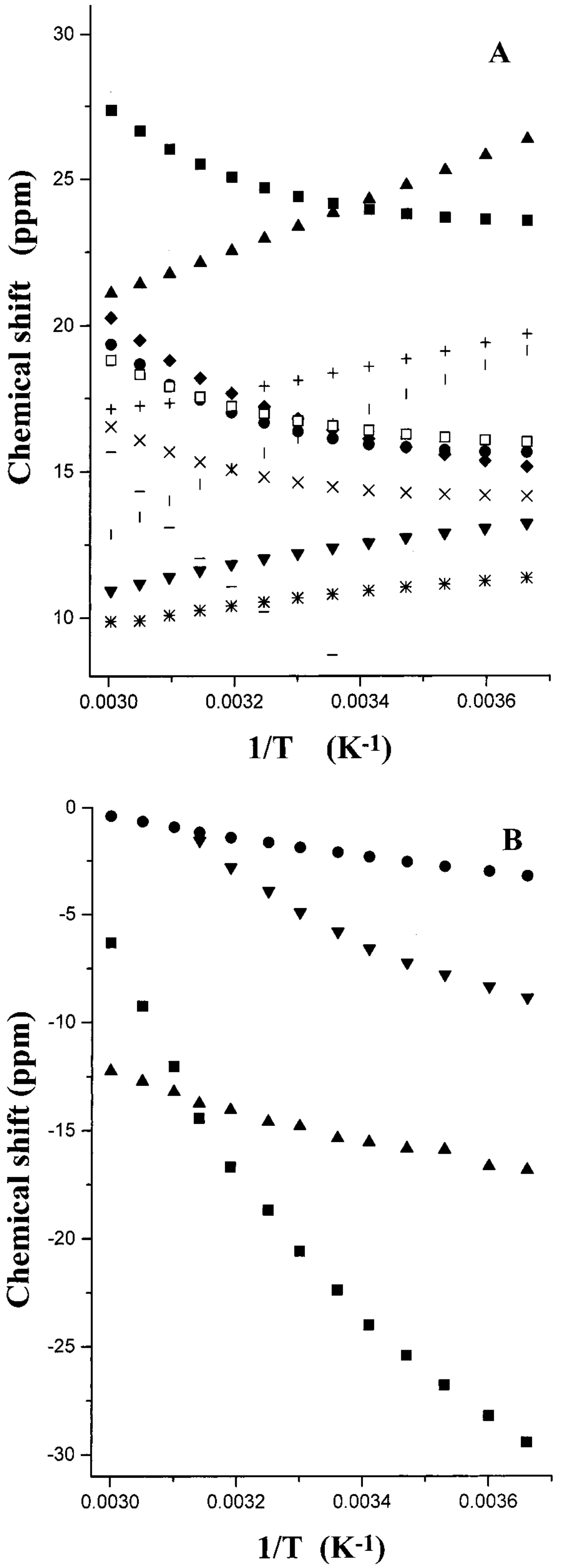

FIGURE 3: Plots of the observed chemical shifts versus reciprocal absolute temperature of oxidized R98C cyt b_{562} at pH = 4.8 in 500 mM phosphate buffer. Panel A: (■) 5-CH_3, (●) 3-CH_3, (▼) HN Met7, (□) 6-H^{α}, (◆) 1-CH_3, (×) 6-$H^{\alpha'}$, (*) HN His102, (−) 8-CH_3, (+) $H^{\beta'}$ His102, (▲) H^{β} His102, and (|) H^{β} Met7. Panel B: (■) H^{γ} Met7, (●) 7-$H^{\beta'}$, (▲) $H^{\epsilon 1}$ His102, and (▼) ϵ-CH_3 Met7.

and all the expected ^{15}N resonances were assigned. The ^{1}H and ^{15}N resonance assignments are reported in the Supporting Information.

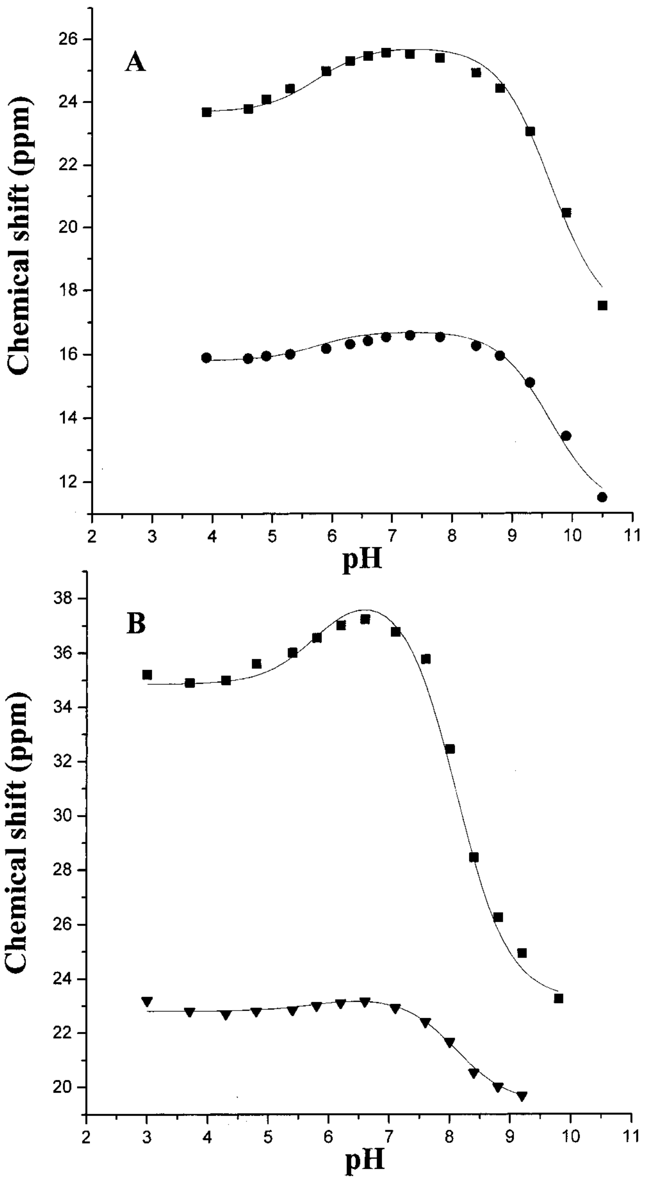

FIGURE 4: pH dependence of the chemical shifts of selected resonances in the R98C cyt b_{562} (A) variant and in wild-type cyt b_{562} (B). The samples were in 500 mM phosphate buffer. The fitting curves are also shown. Panel A: (■) 5-CH_3, and (●) 3-CH_3. Panel B: (■) 5-CH_3 and (▼) 1-CH_3.

Secondary Structure from NMR Data. The elements of secondary structure can already be identified by analyzing the pattern of assigned NOEs (*53*). Short- and medium-range NOEs were used to generate Figure 5. In the present case, four elements of helical secondary structure can be predicted that are characterized by a high number of sequential and medium-range connectivities such as $d_{NN}(i, i + 1)$, $d_{NN}(i, i + 2)$, $d_{\alpha N}(i, i + 3)$, $d_{\alpha N}(i, i + 4)$, and $d_{\alpha\beta}(i, i + 3)$. The four helices involve residues 3−19, 23−41, 57−82, and 84−103. These are commonly referred to as helices α1, α2, α3, and α4 and constitute the well-known four-helix bundle structure of cyt b_{562} (*15*, *54*, *55*). The region involving residues 50−58 constitutes a long loop between helices α2 and α3. The other helices are connected by shorter loops.

Figure 5 also shows residues whose backbone and side-chain NH protons were still observable, with full or partial intensity, after the sample had been dissolved in D_2O for 3 days. These NH protons, therefore, belong to regions of the

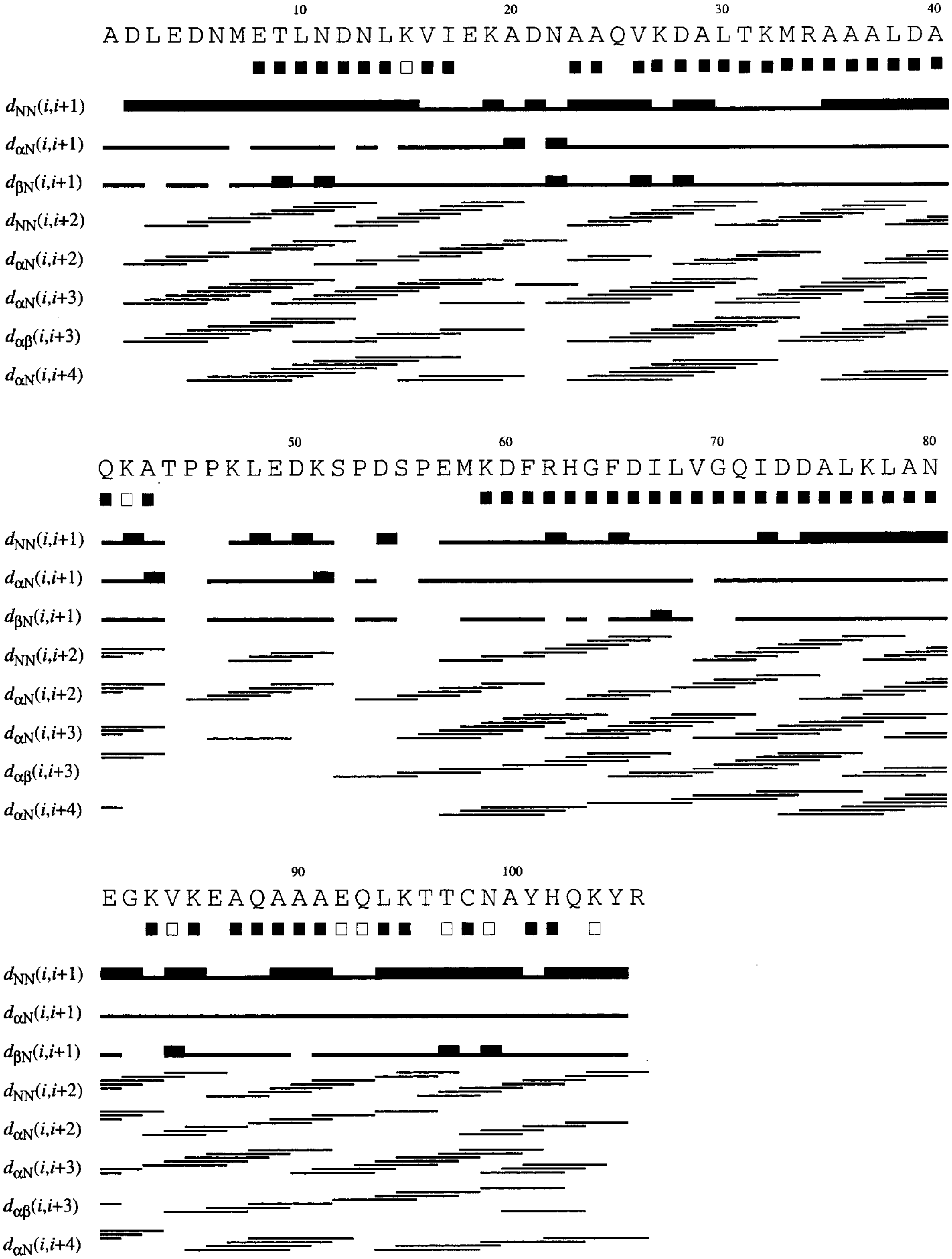

FIGURE 5: Schematic representation of the sequential and medium-range NOE connectivities involving NH, Hα, and Hβ protons for the oxidized form of R98C cyt b_{562}. The thickness of the bar indicates the intensity of NOEs. Filled squares (■) HN protons that are not exchanged after 3 days in D_2O (see text for details); (□) represent partially exchangeable HN protons.

protein that are not accessible to the solvent or which do not experience enough motion, to produce transient solvent accessibility. Most HN protons in the sequential stretches formed by residues 8−17 (helix α1), 23−43 (besides residue 25, helix α2), and 59−80 (helix α3) do not exchange or only partially exchange with solvent. This is consistent with the presence of stable α-helices in those regions, in agreement with the observed NOE patterns. In the region 83−104 (helix α4), the amide protons of some residues are completely exchangeable (86, 96, 100, and 103) while others are partially exchangeable (84, 92, 93, 97, 99, and 104). This suggests that this helix is more solvent-accessible than the other three, possibly as a result of greater mobility. The longest stretch of exchanging backbone amide protons is that of residues 44−58, which includes the long loop between α helices 2 and 3, whereas the second longest involves the N-terminus of the protein, spanning residues 2−7.

The side-chain NH protons are all exchangeable except those of residues Gln 25, Asn 80, and Asn 99.

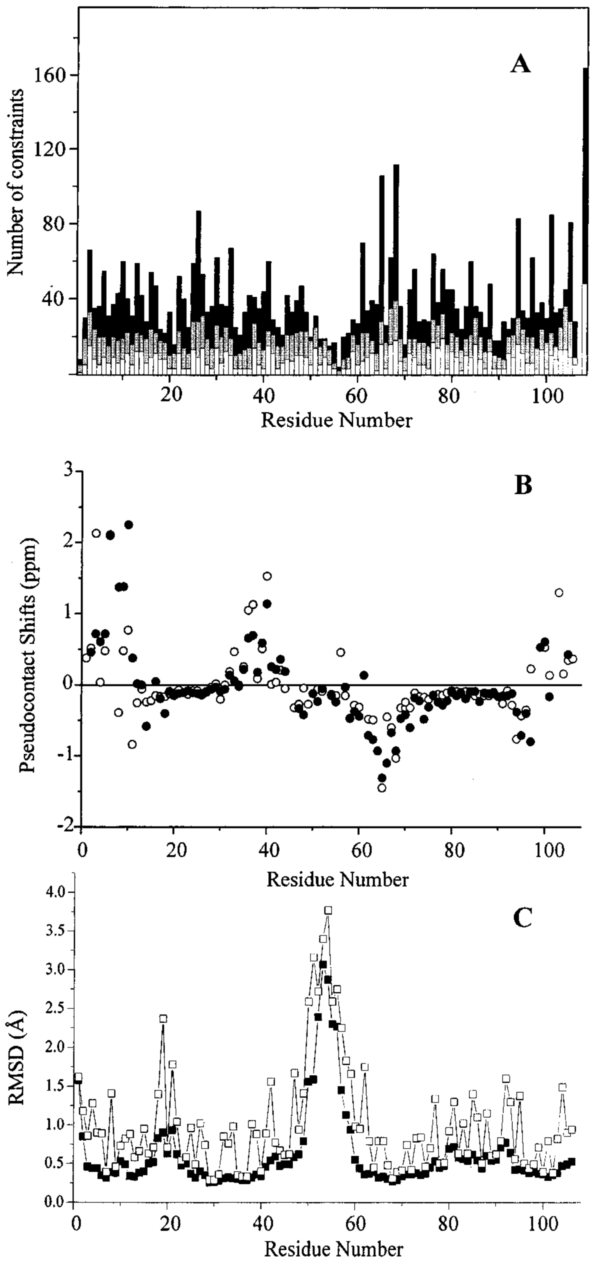

FIGURE 6: Number of meaningful NOE constraints (A) and magnitude of the pseudocontact shifts for HN (●) and H^α (○) protons (B) for each residue for oxidized *E. coli* R98C cyt b_{562}. White, gray, and black bars indicate intraresidue, sequential, and medium/long-range connectivities, respectively. NOEs involving the heme moiety are indicated in the last column on the right. (C) RMSD per residue to the mean structure of oxidized *E. coli* R98C cyt b_{562} for the backbone (■) and all heavy atoms (□) of the PSEUDOREM family of 35 conformers.

Solution Structure Calculations and Analysis. In total, 4325 NOESY cross-peaks were assigned and integrated. These were transformed into upper distance limits with the program CALIBA. Twenty-three distance constraints were derived from 1D NOE experiments involving fast-relaxing paramagnetic shifted signals. Together, these provided 2595 upper distance limits, of which 2145 were found to be meaningful (nonmeaningful distance constraints are those that cannot be violated in any structure conformation and those involving proton pairs at fixed distance). The number of NOEs per residue is reported in Figure 6A. The average number of NOEs per residue is 24 for R98C cyt b_{562}, of which 20 are meaningful. In addition to the above-mentioned NOE constraints, 45 $^3J_{HNH\alpha}$ couplings obtained from the HNHA 3D spectrum and 397 pcs were used for the structure calculations. To evaluate the pcs contribution to the observed chemical shifts of oxidized R98C cyt b_{562}, the chemical shifts of the reduced species are required. The latter can be calculated with the program SHIFT (*56*) with a procedure similar to that already reported (*15*). The assignment of the reduced protein is in progress. For those protons already assigned in the reduced form, the RMSD between calculated and experimental shifts, for both labile and nonlabile protons, was around 0.15 ppm. This is well within the chosen tolerance of 0.5 ppm. The pcs values for HN and Hα protons are reported for each residue in Figure 6B.

Hydrogen-bond constraints for 39 amide protons were used at later stages of structural calculations. A total of 54 proton pairs were stereospecifically assigned through the program GLOMSA. The constraints used for structure calculations and the obtained stereospecific assignments are reported in the Supporting Information.

The 35 conformers constituting the final PSEUDYANA family have an average target function of 0.75 ± 0.15 $Å^2$ and an average backbone RMSD to the mean structure of 0.72 ± 0.12 Å. When the disordered region formed by residues 51−61 is excluded, the average backbone RMSD drops to 0.52 ± 0.07 Å.

The family of structures was then subjected to further refinement with the program AMBER (*45*). The PSEUDOREM family has a total penalty function of 77 ± 19 kJ mol^{-1}, corresponding to an average target function of 0.32 $Å^2$. The NOE contribution is 0.27 $Å^2$ while the pcs contribution is 0.05 $Å^2$. When the entire protein is considered, the average RMSD values for the family are 0.71 ± 0.13 Å for the backbone and 1.18 ± 0.10 Å for the heavy atoms. These values become 0.50 ± 0.07 Å and 1.01 ± 0.08 Å when residues 51−61 are excluded. The RMSD values per residue of the final PSEUDOREM family to the mean structure are shown in Figure 6C. The largest backbone RMSD values are obtained for residues 50−58; the rest of the protein is, on the contrary, well-defined. The high RMSD values of residues 50−58 is due to the paucity of NOEs in this region (Figure 6A) that constitutes the loop connecting helices α2 and α3. This loop is an external, flexible, and unstructured part of the protein, intrinsically poor in the number of observable NOEs. In addition, this region contains two prolines, which break up the sequential connectivities. This region is also disordered in the solution (*15*) and X-ray (*55*) structures of the WT protein. The backbone atoms of the PSEUDOREM family together with the heme and axial ligands are shown in Figure 7.

The final family of conformers was analyzed with PROCHECK-NMR (*49*) and results are reported in Table 3. According to this program, helical structures were found for residues 3−18 (α1), 23−40 (α2), 46−48 (3_{10}), 58−80 (α3), and 84−102 (α4). The secondary structure elements in the energy-minimized mean structure involve residues 2−19 (α1), 22−41 (α2), 45−49 (3_{10}), 57−81 (α3), and 83−103 (α4). Analysis of the NOE patterns leads to a similar conclusion (see above). The data presented in Figure 7 suggest that all the four α-helices are very well defined, with an average backbone RMSD lower than 0.5 Å, whereas in the wild-type protein the N-terminal part of helix α3 was

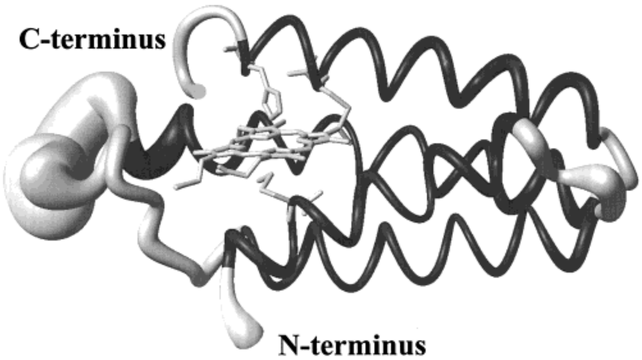

FIGURE 7: Backbone atoms for the solution structure of oxidized *E. coli* R98C cyt b_{562} as a tube with variable radius, proportional to the backbone RMSD of each residue. The figure was generated with the program MOLMOL (*82*).

rather poorly defined with a higher average RMSD value for residues 58−80 (0.82 Å versus 0.42 Å for the present protein), due to the low number of NOE constraints in this region. Furthermore, the average backbone RMSD value for residues 50−58 constituting the external loop is 1.8 Å in R98C cyt b_{562} and 2.5 Å in R98C cyt b_{562} and WT cyt b_{562}. These results indicate that the loop between α2 and α3 (residues 50−58) of the protein, which is found to be highly disordered in the WT cyt b_{562}, is less disordered in the present variant. This behavior is supported by the observation of significantly more NOEs for the 51−61 region in R98C cyt b_{562} (15 per residue) with respect to the WT cyt b_{562} (7 per residue). Furthermore, the NOEs between protons at fixed distances in this loop have lower intensity in WT than in the R98C variant.

The heme group has essentially the same orientation as in the solution structure of the WT protein (Figure 8A). Also the axial ligands of the iron ion (His 102 and Met 7) have a conformation very close to that found in the WT protein. The Met 7 side chain has the same orientation as that found in the crystal structure, taking into account the uncertainty of ±12° on the position of the Met side chain in the solution structure. The His 102 plane in solution deviates about 15° from the orientation in the WT crystal structure. Despite an uncertainty of ±12° (at 3σ) in the orientation of the axial ligand, it seems that the conformation of the iron-coordinated histidine is different in the protein in solution compared with that in the crystal lattice.

The present family of conformers has ca. 88% of the residues in the most favored regions of the Ramachandran plot and ca. 12% in the allowed regions. No residues were in the disallowed regions. In the energy-minimized average structure, 93% of the residues are in the most favored regions of the Ramachandran plot and 7% of the residues are in the allowed regions.

Magnetic Susceptibility Tensor and Contact Shift Pattern. The final $\Delta\chi_{ax}$ and $\Delta\chi_{rh}$ values are $(2.18 \pm 0.08) \times 10^{-32}$ m^3 and $(-0.43 \pm 0.10) \times 10^{-32}$ m^3, respectively. The *z* axis of the magnetic susceptibility tensor deviates slightly from the normal to the heme plane, making an angle of about 8° with it. The projection of the *x* axis on the heme plane makes an angle of about 30° with the N(pyrrole II)−N(pyrrole IV) direction. The arrangement of the tensor with respect to the heme moiety and the ligands is shown in Figure 9A. In WT cyt b_{562}, the tilt of the *z* axis of the magnetic susceptibility tensor is about 20° and the *x* axis makes an angle of 27° with the N(pyrrole II)−N(pyrrole IV) direction, as reported in Figure 9B. The $\Delta\chi_{ax}$ value for the WT cyt b_{562} ($\Delta\chi_{ax} = 1.6 \times 10^{-32}$ m^3) is lower than for the present protein. The increased axial anisotropy in R98C cyt b_{562} is consistent with the larger anisotropy measured for the ground state, through EPR. The present value of $\Delta\chi_{ax}$ is close to that found in

Table 3: Statistical Analysis of the Final PSEUDOREM Family and the Mean Structure of Oxidized R98C Cyt b_{562} from *E. coli*[a]

	PSEUDOREM (35 structures)	⟨PSEUDOREM⟩
RMS Violations per Experimental Distance Constraint[b] (Å)		
intraresidue (361)	0.0143 ± 0.0024	0.0128
sequential (480)	0.0104 ± 0.0025	0.0082
medium-range[c] (802)	0.0070 ± 0.0023	0.0050
long-range (502)	0.0096 ± 0.0020	0.0062
total (2145)	0.0103 ± 0.0017	0.0078
Average Number of Violations per Structure		
intraresidue	10.7 ± 3.1	8
sequential	8.1 ± 2.4	7
medium-range[c]	8.2 ± 2.1	6
long-range	7.8 ± 1.8	5
total	34.9 ± 5.2	26
average no. of NOE violations larger than 0.3 Å	0.03 ± 0.17	0
average no. of ϕ violations larger than 5°	1.1 ± 0.85	1
largest residual NOE violation (Å)	0.46	0.12
RMS violation per pseudocontact shift (ppm)	0.0006 ± 0.0001	0.0004
average NOE and pcs penalty function (kJ mol^{-1})	77 ± 19	50
Structural Analysis[d]		
% of residues in disallowed regions	0.0	0.0
% of residues in generously allowed regions	0.0	0.0
% of residues in allowed regions	12.2	7.2
% of residues in most favorable regions	87.8	92.8

[a] PSEUDOREM indicates the energy-minimized family of 35 structures. ⟨PSEUDOREM⟩ is the energy -minimized average structure obtained from the coordinates of the individual PSEUDOREM structures. [b] The number of experimental constraints for each class is reported in parentheses. [c] Medium-range distance constraints are those between residues (*i*, *i* + 2), (*i*, *i* + 3), (*i*, *i* + 4), and (*i*, *i* + 5). [d] As it results from the Ramachandran plot analysis.

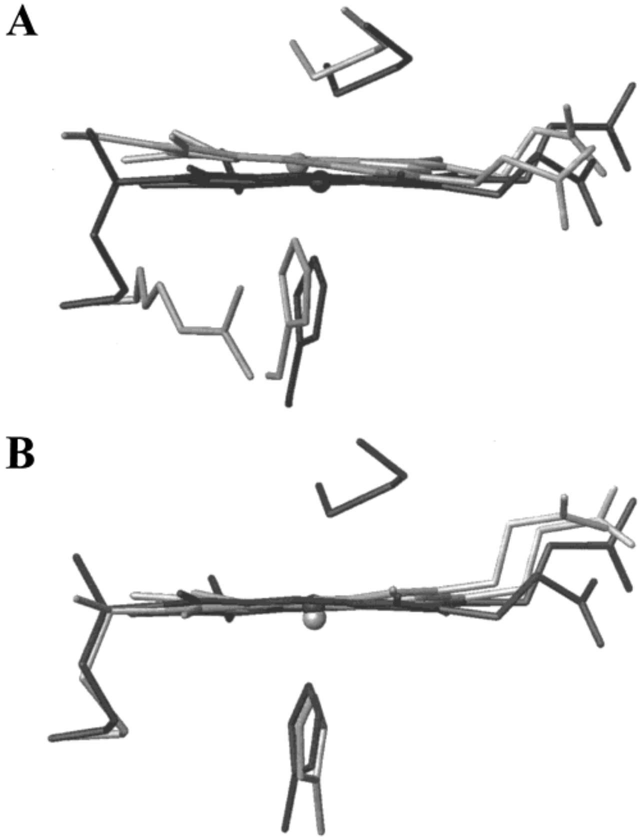

FIGURE 8: (A) View of the heme, the axial ligands, and residue 98 in the average structures of wild-type cyt b_{562} (light gray) and the variant R98C cyt b_{562} (black). (B) Comparison between the heme groups and one cysteine conformation in R98C cyt b_{562} (black) and cyt c' from *R. palustris* (1a7v) (light gray).

c-type cytochromes (*46*, *57*) (in horse heart cytochrome *c*, $\Delta\chi_{ax} = 2.68 \times 10^{-32}$ m^3, and in *Saccharomyces cerevisiae* cytochrome *c*, $\Delta\chi_{ax} = 2.22 \times 10^{-32}$ m^3).

It has been established that the directions of the magnetic susceptibility tensor axes are determined by the relative arrangement of the side chain of the axial ligands (*58*, *59*, *51*). Indeed, a single axial ligand (e.g., His bound to the iron ion) gives rise to an asymmetric π interaction with the metal ion, and the *y* axis of the magnetic susceptibility tensor coincides with the normal to the His plane when the latter is aligned along the N(pyrrole II)−N(pyrrole IV) direction. Otherwise the *x* axis of the magnetic susceptibility tensor rotates clockwise, with respect to the above direction, when the His plane rotates counterclockwise, by essentially the same angle (*52*, *60*−*62*). The same would hold if a methionine is the single axial ligand, with the nodal plane of the lone pair of sulfur taking the place of the His plane. When there are two axial ligands, as in the present case, the two effects sum up, scaled by the relative strength of their π interaction with the iron ion. In the case of cyt *c* the His plane makes an angle of 41° with the N(pyrrole II)−N(pyrrole IV) direction, whereas the nodal plane of the lone pair of the sulfur atom of the Met makes an angle of −56° with the same direction. By simply averaging the two angles, one would expect the *x* direction of the magnetic susceptibility anisotropy tensor to make an angle of 7° with the N(pyrrole II)−N(pyrrole IV) direction, which is in agreement, within the experimental error, with the observed value of 12°. In the case of cytochromes b_5 an analogous relationship is found when the bisecant of the acute angle between the two axial His planes is considered (*62*, *63*). In the present system the angle between the bisector of the His plane and the nodal plane of Met with the N(pyrrole II)−N(pyrrole IV) direction is about 10°, while the *x* direction of the magnetic susceptibility tensor is −30°. The same large deviation holds for WT cyt b_{562}. This odd behavior can be ascribed to the peculiarity of the iron−Met bond in this protein, which is possibly related to the accessibility of $S > {}^1/_2$ electronic states.

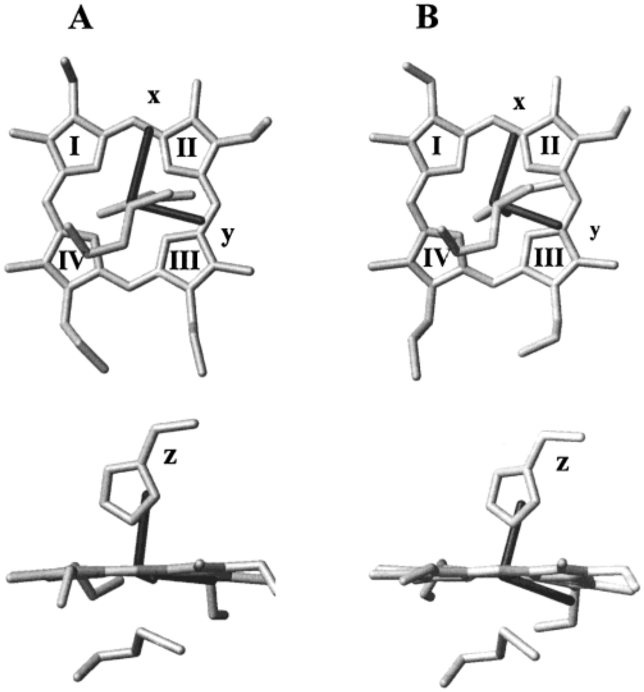

FIGURE 9: Orientation of the magnetic susceptibility anisotropy axes in oxidized *E. coli* R98C cyt b_{562} (A) and in the WT cyt b_{562} (B) with respect to the heme moiety.

The deviation of the *z* axis from the normal to the heme plane is small in the present variant (8°), consistent with the fact that both the Fe−Nϵ2 and the Fe−Sδ bonds are essentially orthogonal to the heme plane (within 2−3°). This holds both in the X-ray and in the present solution structure. Similar deviations had already been reported for other *c*-type cytochromes (*46*, *57*).

Once the magnetic susceptibility anisotropy tensor is available, it is possible to separate the contact and pseudocontact contributions to the hyperfine shifts of the heme substituents and of the ligand protons (*46*). The results are shown in Table 2 together with the chemical shifts of reduced R98C cyt b_{562} previously assigned (*11*), which are necessary to estimate the hyperfine shift. We can see that the smaller shifts for the 5,8,1-heme methyls observed in the R98C cyt b_{562} with respect to the wild-type form are essentially due to a decrease in the contact contribution. This indicates a reduced spin density on the heme in the present protein with respect to the WT protein.

EPR of R98C Cytochrome b_{562}. The 15 K EPR spectra of the wild type and the variant cyt b_{562} are given in Figure 10, panels A and C, respectively. The wild-type protein gives a spectrum that can be simulated through a *g*-strain-broadened $S = {}^1/_2$ system (Figure 10B), giving the *g* values of a low-spin species: $g_z = 3.00$, $g_y = 2.20$, and $g_x = 1.40$. The EPR

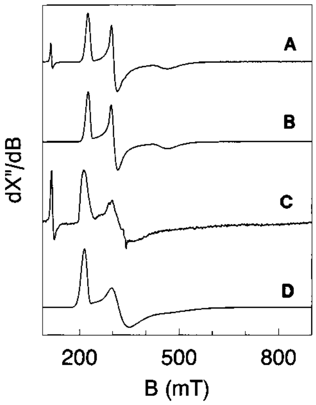

FIGURE 10: EPR spectrum (A) and simulation (B) of the wild-type ferricytochrome b_{562} in 500 mM phosphate buffer, pH 4.8, and EPR spectrum (C) and simulation (D) of the R98C cyt b_{562} in 500 mM phosphate buffer, pH 4.8.

spectrum of R98C cyt b_{562} is significantly different from that of the wild type, and the *g* values are $g_z = 3.15$, $g_y = 2.05$, and $g_x = 1.1$. As mentioned above, EPR spectra at low temperature detect only a single spin state. The variant has increased *g*-anisotropy, indicating a significant change in the electronic structure around the iron. Note that the EPR spectra of the variant have broader features than those of wild type, in particular in the g_z value. This could be the result of shorter relaxation times of the metal ion. This interpretation is also consistent with the decrease in the ^{1}H NMR line widths of the CH_3 signals. The wild-type cyt b_{562} gives also a high-spin signal at $g = 6.00$, as previously detected (*50, 64*). This high-spin signal is not observed in the variant.

DISCUSSION

The solution structure of oxidized *E. coli* R98C cyt b_{562} consists of four long α-helices, packed together in an antiparallel fashion (Figure 7). This arrangement corresponds to the well-known four-helix bundle topology. The iron of the heme cofactor is coordinated in the axial positions by residues in helices α1 and α4. The overall folding of R98C cyt b_{562} is essentially identical to that observed for WT cyt b_{562} in crystal (PDB entry 256B) (*55*) and in solution (*15*). The WT and the R98C variant structures have been compared by superimposing their average energy-minimized structures and thus calculating the RMSD values between the two. Subsequently, these values have to be compared with the RMSD values of the conformers of the two families to the average structures. The global RMSD values between the two averaged minimized structures are 1.12 and 1.50 Å for backbone and heavy atoms, respectively. The RMSD per residue is reported in Figure 11 (— • —) and it is compared to the RMSD per residue for each family [WT (···) and variant (—)] and the sum of the RMSD values of the two families (- - -). As can be seen in Figure 11, the structure definition within each family of structures is very good overall and comparable between the two families. Consequently, a meaningful comparison can be undertaken.

The first observation that can be made is that there are some regions of the protein where the RMSD between the two average minimized structures is larger than the RMSD of each family when the whole structures are superimposed (Figure 11). For the most part these differences in RMSD values originate from some small global translational displacement of helices (Figure 12) while their local conformations are well maintained. However, three regions, which include residues 28−34, 64−67, and 97−100, show a difference in the local RMSD. These local differences are due to small variations of dihedral angles. The helical structure is maintained near the mutation (residues 97−100) without any distortion. In fact, the backbone has moved slightly away from the heme moiety in order to accommodate the thioether linkage. In the WT protein, residue 98 is an arginine and its positively charged side chain points toward the solution. Among the backbone atoms, the Cα atom of Cys 98 (1.3 Å) exhibits the maximum deviation from the position in the WT protein. The axial ligands in the variant remain essentially in the same orientation as in the WT cyt b_{562} (Figure 8A) besides small-angle changes within the experimental uncertainty (±12° at 3σ). This has been confirmed by a large number of NOE connectivities derived by 2D NOESY and 1D NOE experiments for the most hyperfine-shifted signals (see Supporting Information). It is interesting to note a rotation of the imidazole ring observed in both variant and WT solution structures with respect to the X-ray structure of WT cyt b_{562}.

The helices are well-defined in both WT and the present variant of cyt b_{562}, with backbone RMSD values of 0.3−0.4 Å. However, in WT cyt b_{562} helix α_3 is not as well-defined as the others. This helix follows the long external loop encompassing residues 50−58, which represents the most disordered region of the protein (RMSD 2.5 Å). In the R98C variant the loop and helix α_3 are more defined (RMSD 1.9 and 0.4 Å, respectively) due to a larger number of NOE constraints. This increased order might be the result of an increased rigidity in the R98C structure. This is supported by the NOE intensity ratios for some protons at fixed distances belonging either to the well-defined regions or to the loop. In WT cyt b_{562} the NOE intensities in the latter region are significantly reduced. Furthermore, the loop and helix α_3 show a smaller number of long-range NOEs. The increased rigidity in R98C cyt b_{562} might be the result of the thioether linkage that fixes the heme cofactor within the protein frame. The chemical equilibrium between the two heme orientations, as it occurs in the WT cyt b_{562}, may be the cause of the increased disorder of this region of the WT protein.

While the structural differences between WT cyt b_{562} and the present variant are very small, significant changes in the stability are observed between the two proteins. The covalent attachment of heme to the cytochrome b_{562} polypeptide clearly stabilizes the protein toward both chemical and thermal unfolding. Even though it is difficult to quantify this effect at this stage, it is clear from these initial results that the denatured states of the WT and R98C proteins are significantly different. The optical spectrum of the denatured R98C suggests that the heme is in a somewhat structured environment. Qualitatively similar spectra (Soret at 407/408 nm) are observed for mitochondrial cytochrome *c* at neutral pH in either urea-, or GdnHCl-denatured states (*65, 66*), which have been shown to contain bis-histidine-coordinated heme iron (*67*). These spectra are red-shifted from those of *c*-type heme in the absence of significant polypeptide, such as the cytochrome *c* fragments, microperoxidase 8 and 11, in which the Soret peaks are at 396 nm (*65*). The spectrum of GdnHCl-denatured R98C cyt b_{562} is slightly different from

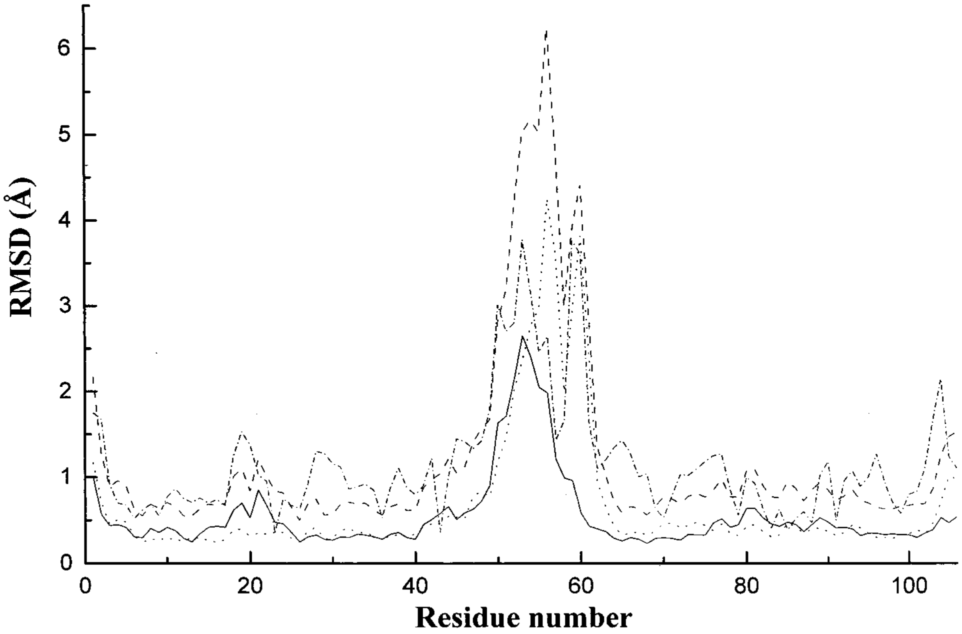

FIGURE 11: RMSD per residue (for backbone atoms) between the conformers of the family of (···) oxidized WT cyt b_{562} (taken from ref *15*), (—) oxidized R98C cyt b_{562}, and (—•—) RMSD between the mean structures of the two families. The sum of the RMSD values per residue for the two families of structures is also shown (---).

FIGURE 12: Backbone drawing of oxidized cyt b_{562} in its wild-type form (light gray) and of the variant R98C cyt b_{562} (black). The heme is reported and the position of the Cα carbon atom of residue 98 is shown with arrows.

that of similarly denatured cytochrome *c*, in that the former has a high-spin marker band at 620 nm. Additionally, the slope (*m*) of the ΔG dependence on [GdnHCl] for each protein is significantly different. The value of 14.2 kJ mol^{-1} M^{-1} for the WT protein is approximately that expected for a protein of this size and is consistent with the urea denaturation published previously (*68*). The value of 8.4 kJ mol^{-1} M^{-1} for the R98C variant is significantly lower and suggests that, upon denaturation of this variant, there is a smaller increase in the exposure of the polypeptide to denaturant than occurs with the WT protein. Given that the structures of the native states of the WT and R98C proteins are very similar, these data suggest that the R98C variant has significant residual structure in 7.2 M GdnHCl. It has been noted that heme binds to the thermally denatured WT protein with a predicted dissociation constant of 3 μM (*9*), suggesting that this protein state also may have significant residual structure. However, the same may not be true for the chemically denatured WT protein. The origins of the increase in stability upon introduction of the covalent linkage will therefore be difficult to ascertain from conventional folding studies. We would predict that there should be an entropic destabilization of the denatured state of the R98C with respect to the WT protein due to the significant residual structure. This may provide an increase in free energy of folding upon introduction of the covalent linkage, although the observed increase in rigidity/ordering of the native state due to this modification may also decrease the entropy of this state and limit the overall stabilization that is observed. It will be very interesting to obtain structural and dynamic information about the denatured state of R98C cyt b_{562} by NMR spectroscopy, which would provide key information in the understanding of this system.

How does the structure at the site of covalent linkage compare with similar thioether linkages observed in cytochromes *c*′? The data presented here confirm the stereochemistry at the heme 2α carbon to be *S*, in common with all other cytochromes *c* (*13*, *69*), as already suggested (*11*). We have superimposed the five atoms of pyrrole B of the heme in the average structure of R98C cyt b_{562} with those of X-ray structures of *c*-type cytochromes, like horse heart (PDB entry 1HRC) (*70*) and yeast (PDB entry 2YCC) (*71*) cytochrome *c*, and then compared the conformations of the cysteine side chains attached to the 2α carbon of the heme. Further comparison is done with cytochromes *c*′ for which structures are known.[2] The cysteine side-chain conformations in all of these cases are essentially identical. The comparable bond and torsion angles fall within a 10° spread. The superinposition places the Cα carbon of the cysteine residues within 0.8 Å of each other. Figure 8B shows the superimposition of R98C cyt b_{562} and cytochrome *c*′ and the linkage to the heme.

These small differences are interesting in the context of the formation of the covalent bond between the cysteine thiol and the heme 2-vinyl group within the cytochrome b_{562} scaffold. We have not found any conditions under which this linkage will form spontaneously in R98C cyt b_{562}, while the linkage is readily formed *in vivo* (*11*) and enzymatically *in vitro* (*21*). Given the small structural differences between the R98C and WT structures, it is surprising that no spontaneous reaction is observed. This is especially true given that spontaneous formation of a thioether linkage has been observed between cysteine residues at position 101 and the 2-vinyl group of the heme in the alternative heme orientation (B) (*11*). The expected electrophilic addition reaction mechanism involves the protonation of the vinyl Cβ atom before attack of the cysteine thiolate on the resulting cationic center at the vinyl Cα position. It may be that the reaction is controlled by the availability of the initial proton, the source of which is unknown. It will be interesting to examine the backbone and side-chain dynamics in this region of the protein. Although the averaged structures of the protein in "substrate" (WT cyt b_{562}) and "product" (R98C cyt b_{562}) states are similar, they are not identical and there may be too little conformational flexibility around the heme binding site for the transition state to be attained.

The ^{1}H shift separation of the heme moiety of the variant is quite different compared to the wild type, with 5- and 8-CH_3 well separated and 1- and 3-CH_3 close to one another. Generally, in low-spin heme proteins methyls 1,5 and 3,8 have different pairwise shifts (*63*) even if they experience similar values when the molecular in plane axes are along the *meso* protons. WT cyt b_{562} follows this rule, with the 5-CH_3, 1-CH_3 resonances having large shifts and the 8-CH_3, 3-CH_3 slight shifts. The different behavior of the present variant with respect to the wild-type protein cannot be due to a different orientation of the axial ligands, as they are essentially the same. On the other hand, the presence of the covalent bond must be taken into account. The pattern of the heme CH_3 shifts has been related to the orientation of the two axial ligands (*52*, *60*, *72*). The π orbitals of the axial ligands interact with the d_{xz} and d_{yz} orbitals of the metal ion with suitable symmetry, thus determining a pairwise spin delocalization on the opposite pyrroles. Generally the 1- and 5-methyl groups give as close resonances as the 3- and 8-methyls do. In the WT cyt b_{562}, there is a large difference between 1-CH_3 and 5-CH_3 shifts, although the latter shifts are larger than those of the 3,8 pair. In the present variant, the shifts of the 1-, 5-, and 8-CH_3 are much lower with respect to the WT cyt b_{562}, while that of 3-CH_3 is almost the same. To justify the large variation upon mutation, we should consider the effect of chemical modification in position 2 of the heme. It has been recently proposed that the heme substituents in position 2 and 4 play an important role in determining the pattern of spin delocalization on the heme ring (*73*). It was suggested that the peripheral heme substituents contribute to the energy separation of the d orbitals, thus affecting the spin density distribution. The present variant contains both vinyl and thioether groups as heme substituents. This mixture of substituents introduces an asymmetry on the heme, which dramatically changes the spin delocalization on it. The present finding confirms that the CH_3 shift pattern is determined not only by axial ligands but also by the nature of the heme substituents, in particular those on positions 2 and 4. The data are therefore quite relevant for the correlation between molecular and structural properties and spin delocalization patterns. The other striking difference in the comparison between the present variant and WT protein is the difference in the absolute value of the shift of the heme resonances that may indicate a difference to the overall paramagnetism. Cytochromes *c* with His/Met axial ligands provide hyperfine shift patterns that are not fully understood in detail (*52*). Spin equilibrium with $S > {}^1/_2$ has been invoked on several occasions (*51*, *52*). Such spin equilibrium in WT cyt b_{562} is dramatic, while the behavior of this variant is closer to that of cytochromes *c*, with a lower accessibility to $S > {}^1/_2$ states. Even the magnetic susceptibility anisotropy is intermediate between that of WT and that of cyt *c*. The EPR spectra indicate a higher anisotropy for the ground state in R98C cyt b_{562} with respect to wild-type protein. The *g*-anisotropy in the present variant is more similar to that found for some *c*-type cytochromes (*74*).

pH-Dependent Properties of the Solution Structure. The pH-dependent spectroscopic properties of the wild-type form of cyt b_{562} have been reported previously (*50*). This work showed that the pH-dependent changes in the chemical shift of the hyperfine-coupled signals in the ^{1}H NMR spectra can be accounted for by the presence of two titratable groups. The reduction potentials were also found to be pH-dependent, with the presence of three acid−base equilibria coupled to the oxidation state (*75*). These have been attributed to the ionization of heme propionate 7, of the iron-bound histidine, and possibly to the ionization of a carboxylate group for the pK_a below 5. In the present variant the second, higher pK_a is about 1.5 units higher than in WT protein. This large difference can be attributed to mutation at position 98. In fact, the positively charged guanidinium group of Arg 98 in

---

[2] Available cytochrome *c*′ structures are *Rhodopseudomonas palustris*, PDB entry 1A7V; *Chromatium vinosum*, PDB entry 1BBH; *Alcaligenes denitrificans*, PDB entry 1CGN; *Alcaligenes* sp., PDB entry 1CGO; *Rhodobacter capsulatus*, PDB entries 1CPQ and 1RCP; *Rhodobacter capsulatus* strain St. Louis, PDB entry 1CPR; *Rhodocyclus gelatinosus*, PDB entry 1JAF; and *Rhodospirillum molischianum*, PDB entry 2CCY.

the WT cyt b_{562} is close to the HN of the ring of the axial histidine (within 5 Å), and can stabilize the negative charge of the histidinate anion. This leads to a decrease in the pK_a value with respect to the value expected for an imidazole group complexed with a heme−iron cofactor (*76*, *77*). The replacement of Arg 98 with a Cys residue in the R98C variant removes the guanidinium group and increases the pK_a close to the value expected for a normal histidine coodinated to heme iron.

The pH dependence of the ^{1}H NMR spectra of cytochromes c′ from *R. gelatinosus* and *C. vinosum* can be accounted for with three pK_a values at about 5, 6.5, and 9.5 (*78*), which have been attributed on the basis of the available X-ray structures (*79*) to the ionization of a carboxylate group, a propionate group, and the axially bound histidine, respectively. In the *R. molischianum* (*80*) and *R. palustris* (*81*) cytochromes *c*′, only the two higher pK_as were observed. It is worth noting that, in cytochromes *c*′, the pK_a value ascribed to the histidinate ionization is similar to that of the present cytochrome b_{562} variant. It is also interesting that these proteins, which adopt a similar fold despite their low homology, also exhibit a very similar ionization behavior, having residues with similar properties surrounding the ionizable groups. These observations might point to a similar biological function for these two classes of proteins.

ACKNOWLEDGMENT

We to thank Professor F. Hagen for performing the EPR experiments and Mr. M. Lucci for help during the acquisition of the NMR spectra. We also thank Dr. A. Rosato for preparing some R98C cyt b_{562} samples.

SUPPORTING INFORMATION AVAILABLE

^{1}H and ^{15}N chemical shifts, experimental NOE intensities used for the structure calculations, list of stereospecific assignments, pseudocontact shift constraints, $^3J_{HNH\alpha}$ coupling constants, and hydrogen-bond constraints. This material is available free of charge via the Internet at http://pubs.acs.org.

REFERENCES

1. *The porphyrins* (1978) Academic Press Inc., London.
2. Kadish, K. M., Smith, K. M., and Guilard, R., Eds. (1999) *The Porphyrin Handbook*, Academic Press, Burlington, MA.
3. Wittung-Stafshede, P., Gray, H. B., and Winkler, J. R. (1997) *J. Am. Chem. Soc. 119*, 9562−9563.
4. Englander, S. W., Sosnick, T. R., Mayne, L. C., Shtilerman, M., Qi, P. X., and Bai, Y. W. (1998) *Acc. Chem. Res. 31*, 737−744.
5. Shastry, M. C. R., Sauder, J. M., and Roder, H. (1998) *Acc. Chem. Res. 31*, 717−725.
6. Yeh, S. R., Han, S. W., and Rousseau, D. L. (1998) *Acc. Chem. Res. 31*, 727−736.
7. Fisher, M. T. (1991) *Biochemistry 20*, 10012−10018.
8. Robinson, C. R., and Sligar, S. G. (1993) *Protein Sci. 2*, 826−837.
9. Robinson, C. R., Liu, Y., Thomson, A. J., Sturtevant, J. M., and Sligar, S. G. (1997) *Biochemistry 36*, 16141−16146.
10. Robinson, C. R., Liu, Y., O'Brien, R., Sligar, S. G., and Sturtevant, J. M. (1998) *Protein Sci. 7*, 961−965.
11. Barker, P. D., Nerou, E. P., Freund, S. M. V., and Fearnley, I. M. (1995) *Biochemistry 34*, 15191−15203.
12. Barker, P. D., Ferrer, J. C., Mylrajan, M., Loehr, T. M., Feng, R., Konishi, Y., Funk, W. D., MacGillivray, R. T. A., and Mauk, A. G. (1993) *Proc. Natl. Acad. Sci. U.S.A. 90*, 6542−6546.
13. Moore, G. R., and Pettigrew, G. W. (1990) in *Cytochromes c; Evolutionary, Structural and Physicochemical Aspects*, Springer-Verlag, Berlin.
14. Banci, L., Bertini, I., Luchinat, C., & Turano, P. (1999) in *The Porphyrin Handbook* (Kadish, K. M., Smith, K. M., and Guilard, R., Eds.) Academic Press, Burlington, MA.
15. Arnesano, F., Banci, L., Bertini, I., Faraone-Mennella, J., Rosato, A., Barker, P. D., and Fersht, A. R. (1999) *Biochemistry 38*, 8657−8670.
16. Arnesano, F., Banci, L., Bertini, I., and Felli, I. C. (1998) *Biochemistry 37*, 173−184.
17. Arnesano, F., Banci, L., Bertini, I., Felli, I. C., and Koulougliotis, D. (1999) *Eur. J. Biochem. 260*, 347−354.
18. Dangi, B., Sarma, S., Yan, C., Banville, D. L., and Guiles, R. D. (1998) *Biochemistry 37*, 8289−8302.
19. Keller, R. M., and Wüthrich, K. (1980) *Biochim. Biophys. Acta 621*, 204−217.
20. McLachlan, S. J., La Mar, G. N., Burns, P. D., Smith, K. D., and Langry, K. C. (1986) *Biochim. Biophys. Acta 874*, 274−284.
21. Rice, J. K., Fearnley, I. M., and Barker, P. D. (1999) *Biochemistry 38*, 16847−16856.
22. Miroux, B., and Walker, J. E. (1996) *J. Mol. Biol. 260*, 289−298.
23. Reid, L. S., Mauk, M. R., and Mauk, A. G. (1984) *J. Am. Chem. Soc. 106*, 2182−2185.
24. Bax, A., and Davis, D. G. (1985) *J. Magn. Reson. 63*, 207−213.
25. Griesinger, C., Otting, G., Wüthrich, K., and Ernst, R. R. (1988) *J. Am. Chem. Soc. 110*, 7870−7872.
26. Kay, L. E., Marion, D., and Bax, A. (1989) *J. Magn. Reson. 84*, 72−84.
27. Macura, S., Wüthrich, K., and Ernst, R. R. (1982) *J. Magn. Reson. 47*, 351−357.
28. Marion, D., and Wüthrich, K. (1983) *Biochem. Biophys. Res. Commun. 113*, 967−974.
29. Banci, L., Bertini, I., Luchinat, C., Piccioli, M., Scozzafava, A., and Turano, P. (1989) *Inorg. Chem. 28*, 4650−4656.
30. Inubushi, T., and Becker, E. D. (1983) *J. Magn. Reson. 51*, 128−133.
31. Rigby, S. E. J., Burch, A. M., and Moore, G. R. (1991) *Magn. Reson. Chem. 29*, 1036−1039.
32. Vuister, G. W., and Bax, A. (1993) *J. Am. Chem. Soc. 115*, 7772−7777.
33. Piotto, M., Saudek, V., and Sklenar, V. (1992) *J. Biomol. NMR 2*, 661−666.
34. Eccles, C., Güntert, P., Billeter, M., and Wüthrich, K. (1991) *J. Biomol. NMR 1*, 111−130.
35. Pierik, A. J., and Hagen, W. R. (1991) *Eur. J. Biochem. 195*, 505−516.
36. Hagen, W. R. (1985) *J. Magn. Reson. 61*, 220−244.
37. Güntert, P., Braun, W., and Wüthrich, K. (1991) *J. Mol. Biol. 217*, 517−530.
38. Bertini, I., and Luchinat, C. (1986) in *NMR of paramagnetic molecules in biological systems*, Benjamin/Cummings, Menlo Park, CA.
39. Bertini, I., & Turano, P. (1994) in *NMR of paramagnetic macromolecules* (La Mar, G. N., Ed.) NATO ASI Series, (La Mar, G. N., Ed.) Kluwer Academic, Dordrecht, The Netherlands.
40. Bertini, I., and Luchinat, C. (1996) in *NMR of paramagnetic substances, Coord. Chem. Rev. 150*.
41. Banci, L., Bertini, I., Cremonini, M. A., Gori Savellini, G., Luchinat, C., Wüthrich, K., and Güntert, P. (1998) *J. Biomol. NMR 12*, 553−557.
42. Güntert, P., Mumenthaler, C., and Wüthrich, K. (1997) *J. Mol. Biol. 273*, 283−298.
43. Banci, L., Bertini, I., Bren, K. L., Cremonini, M. A., Gray, H. B., Luchinat, C., and Turano, P. (1996) *J. Biol. Inorg. Chem. 1*, 117−126.

44. Banci, L., Bertini, I., Gori Savellini, G., Romagnoli, A., Turano, P., Cremonini, M. A., Luchinat, C., & Gray, H. B. (1997) *Proteins: Struct., Funct., Genet. 29*, 68−76.
45. Pearlman, D. A., Case, D. A., Caldwell, J. W., Ross, W. S., Cheatham, T. E., Ferguson, D. M., Seibel, G. L., Singh, U. C., Weiner, P. K., and Kollman, P. A. (1997) *AMBER 5.0*, University of California, San Francisco.
46. Banci, L., Bertini, I., Gray, H. B., Luchinat, C., Reddig, T., Rosato, A., and Turano, P. (1997) *Biochemistry 36*, 9867−9877.
47. Borgias, B., Thomas, P. D., and James, T. L. (1989) *COmplete Relaxation Matrix Analysis (CORMA)*, University of California, San Francisco.
48. Laskowski, R. A., MacArthur, M. W., Moss, D. S., and Thornton, J. M. (1993) *J. Appl. Crystallogr. 26*, 283−291.
49. Laskowski, R. A., Rullmann, J. A. C., MacArthur, M. W., Kaptein, R., and Thornton, J. M. (1996) *J. Biomol. NMR 8*, 477−486.
50. Moore, G. R., Williams, R. J., Peterson, J., Thomson, A. J., and Mathews, A. J. (1985) *Biochim. Biophys. Acta 829*, 83−96.
51. Wu, J. Z., La Mar, G. N., Yu, L. P., Lee, K. B., Walker, F. A., Chiu, M. L., and Sligar, S. G. (1991) *Biochemistry 30*, 2156−2165.
52. Banci, L., Bertini, I., Luchinat, C., Pierattelli, R., Shokhirev, N. V., and Walker, F. A. (1998) *J. Am. Chem. Soc. 120*, 8472−8479.
53. Wüthrich, K. (1986) in *NMR of Proteins and Nucleic Acids*, Wiley, New York.
54. Lederer, F., Glatigny, A., Bethge, P. H., Bellamy, H. D., and Mathews, F. S. (1981) *J. Mol. Biol. 148*, 427.
55. Hamada, K., Bethge, P. H., and Mathews, F. S. (1995) *J. Mol. Biol. 247*, 947−962.
56. Ösapay, K., and Case, D. A. (1991) *J. Am. Chem. Soc. 113*, 9436−9444.
57. Banci, L., Bertini, I., Bren, K. L., Gray, H. B., Sompornpisut, P., and Turano, P. (1997) *Biochemistry 36*, 8992−9001.
58. Shulman, R. G., Glarum, S. H., and Karplus, M. (1971) *J. Mol. Biol. 57*, 93−115.
59. Oosterhuis, W. T., and Lang, G. (1969) *Phys. Rev. 178*, 439−456.
60. Turner, D. L. (1995) *Eur. J. Biochem. 227*, 829−837.
61. Banci, L., Rosato, A., and Turano, P. (1996) *J Biol. Inorg. Chem. 1*, 364−367.
62. Shokhirev, N. V., and Walker, F. A. (1998) *J. Am. Chem. Soc. 120*, 981−990.
63. Shokhirev, N. V., and Walker, F. A. (1998) *J. Biol. Inorg. Chem. 3*, 581−594.
64. Iba, K., Takamiya, K., Nishimura, M., and Itoh, S. (1986) *J. Biochem. (Tokyo) 100*, 1477−1480.
65. Feng, Y. S., and Sligar, S. G. (1991) *Biochemistry 30*, 10150−10159.
66. Babul, J., and Stellwagen, E. (1971) *Biopolymers 10*, 2359−2361.
67. Colon, W., Wakem, L. P., Sherman, F., and Roder, H. (1997) *Biochemistry 36*, 12535−12541.
68. Tsong, T. Y. (1975) *Biochemistry 14*, 1543−1547.
69. Scott, R. A., and Mauk, A. G. (1996) in *Cytochrome c. A multidisciplinary approach*, University Science Books, Sausalito, CA.
70. Bushnell, G. W., Louie, G. V., and Brayer, G. D. (1990) *J. Mol. Biol. 214*, 585−595.
71. Berghuis, A. M., and Brayer, G. D. (1992) *J. Mol. Biol. 223*, 959−976.
72. Karplus, M., and Fraenkel, G. K. (1961) *J. Chem. Phys. 35*, 1312−1323.
73. Kolczak, U., Hauksson, J. B., Davis, N. L., Pande, U., de Ropp, J. S., Langry, K. C., Smith, K. M., and La Mar, G. N. (1999) *J. Am. Chem. Soc. 121*, 835−843.
74. Brautigan, D. L., Feinberg, B. A., Hoffman, B. M., Margoliash, E., Peisach, J., and Blumberg, W. E. (1977) *J. Biol. Chem. 252*, 574−582.
75. Barker, P. D., Butler, J. L., de Oliveira, P., Hill, H. A. O., and Hunt, N. I. (1996) *Inorg. Chim. Acta 252*, 71−77.
76. George, P., Hanania, G. I. H., Irvine, D. H., and Abu-Issa, I. (1964) *J. Chem. Soc.* 5689−5694.
77. Gadsby, P. M. A., and Thomson, A. J. (1982) *FEBS Lett. 150*, 59−63.
78. Banci, L., Bertini, I., Turano, P., and Vicens Oliver, M. (1992) *Eur. J. Biochem. 204*, 107−112.
79. Bertini, I., Gori, G., Luchinat, C., and Vila, A. J. (1993) *Biochemistry 32*, 776−783.
80. Jackson, J. T., La Mar, G. N., and Bartsch, R. G. (1983) *J. Biol. Chem. 258*, 1799−1805.
81. La Mar, G. N., Jackson, J. T., Dugad, L. B., Cusanovich, M. A., and Bartsch, R. G. (1990) *J. Biol. Chem. 265*, 16173−16180.
82. Koradi, R., Billeter, M., and Wüthrich, K. (1996) *J. Mol. Graphics 14*, 51−55.

BI991831O